LETTER

doi:10.1038/nature14515

Global-scale coherence modulation of radiation-belt electron loss from plasmaspheric hiss

A. W. Breneman[1], A. Halford[2], R. Millan[2], M. McCarthy[3], J. Fennell[4], J. Sample[5], L. Woodger[2], G. Hospodarsky[6], J. R. Wygant[1], C. A. Cattell[1], J. Goldstein[7], D. Malaspina[8] & C. A. Kletzing[6]

Over 40 years ago it was suggested that electron loss in the region of the radiation belts that overlaps with the region of high plasma density called the plasmasphere, within four to five Earth radii[1,2], arises largely from interaction with an electromagnetic plasma wave called plasmaspheric hiss[3–5]. This interaction strongly influences the evolution of the radiation belts during a geomagnetic storm, and over the course of many hours to days helps to return the radiation-belt structure to its 'quiet' pre-storm configuration. Observations have shown that the long-term electron-loss rate is consistent with this theory but the temporal and spatial dynamics of the loss process remain to be directly verified. Here we report simultaneous measurements of structured radiation-belt electron losses and the hiss phenomenon that causes the losses. Losses were observed in the form of bremsstrahlung X-rays generated by hiss-scattered electrons colliding with the Earth's atmosphere after removal from the radiation belts. Our results show that changes of up to an order of magnitude in the dynamics of electron loss arising from hiss occur on timescales as short as one to twenty minutes, in association with modulations in plasma density and magnetic field. Furthermore, these loss dynamics are coherent with hiss dynamics on spatial scales comparable to the size of the plasmasphere. This nearly global-scale coherence was not predicted and may affect the short-term evolution of the radiation belts during active times.

We analyse in detail the magnetic conjunctions between the Van Allen probes (a NASA Earth-orbiting satellite mission)[6] and the Balloon Array for Radiation belt Relativistic Electron Losses (BARREL) balloons[7] flying at altitudes of nearly 35 km over Antarctica on 3 and 6 January 2014. We then used this new set of measurements to explore spatial and temporal scales previously not easily accessible. On 2 January 2014, a dynamic injection of energetic electrons (tens of kiloelectronvolts; thought to arise from lower-energy populations beyond the radiation belts) into the outer radiation belt down to at least $L = 3$ occurred. (L is defined as a magnetic field line whose value is the distance in Earth radii (R_E) at which it intersects the magnetic equator.) These electrons, trapped within the plasmasphere, were gradually eroded over the course of a few days by various loss mechanisms, including interaction with plasmaspheric hiss. The hiss on 3 and 6 January has a peak power at frequencies <100 Hz and probably originates from a free-energy source within the plasmasphere[8–10].

Figure 1 plots three hours of detrended hiss and X-ray observations, corresponding to electrons with energies of tens of kiloelectronvolts for an afternoon-sector conjunction between Van Allen probe P_A and balloon B_I on 3 January 2014. For a detailed description of a conjunction see the Methods and Extended Data Fig. 1. During this conjunction B_I stays near the field line $L = 5.2$, which maps to the plasmasphere, while P_A traverses a large extent of the afternoon-sector plasmasphere from $L = 5.5$–2.5. It is immediately evident that there is a strong visible coherence between the hiss amplitude and the X-ray count rate at periods of 1–20 min throughout the conjunction. This coherence extends throughout the entire afternoon-sector plasmasphere, even when P_A and B_I have spatial separations of up to $3L$ and nearly 3 h of magnetic local time (MLT), corresponding to separations across the magnetic field in the range $2.3R_E$–$4.1R_E$, or 14,500–26,000 km.

Similar long-distance coherence was observed for a few days after the energetic particle injection on 2 January. Six payloads (P_A, P_B, B_K,

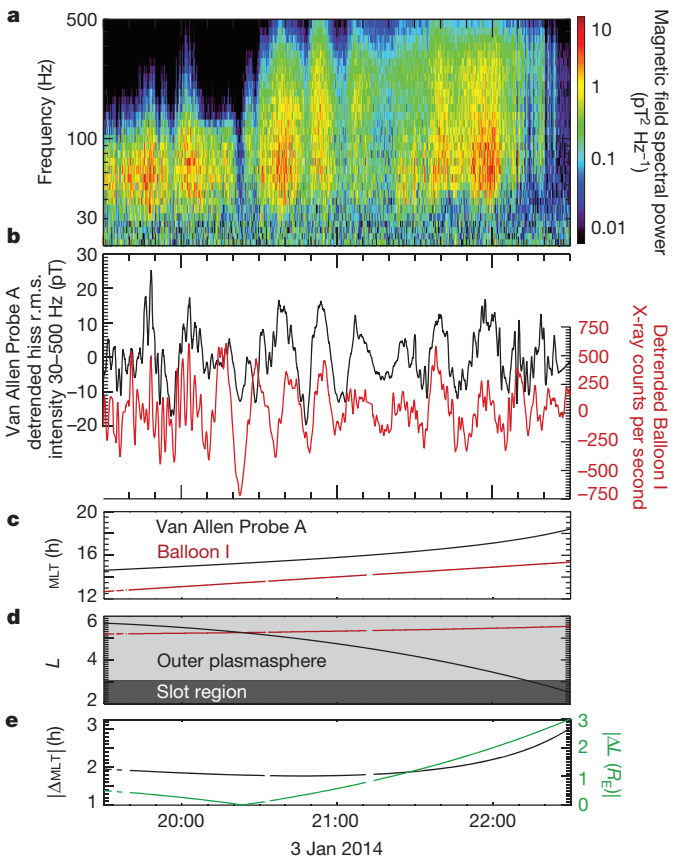

Figure 1 | Comparison of satellite and balloon data showing large-scale coherence. A magnetic field spectrogram (**a**) from the Electric Fields and Waves instrument[10] on P_A shows hiss with peak power at frequencies <100 Hz (ref. 9). The root mean square (r.m.s.) hiss amplitude, up to 20 pT and consistent with quiet-time values[8], shows fluctuations similar to the X-ray count rate on B_I (**b**), caused by electrons of 10–200 keV. Both curves were detrended with a 20-min running boxcar average to emphasize fluctuations. Panels **c**–**e** show the MLT, L, $|\Delta MLT|$ and $|\Delta L|$ values for P_A and B_I.

[1]School of Physics and Astronomy, University of Minnesota, Minneapolis, Minnesota 55455, USA. [2]Department of Physics and Astronomy, Dartmouth College, Hanover, New Hampshire 03755, USA. [3]Earth and Space Sciences, University of Washington, Seattle, Washington 98195, USA. [4]Aerospace Corporation, Los Angeles, California 90009, USA. [5]Space Sciences Laboratory, University of California, Berkeley, California 94720, USA. [6]Department of Physics and Astronomy, University of Iowa, Iowa City, Iowa 52242, USA. [7]Southwest Research Institute, San Antonio, Texas 78238, USA. [8]University of Colorado, The Laboratory for Atmospheric and Space Physics (LASP), Boulder, Colorado 80303, USA.

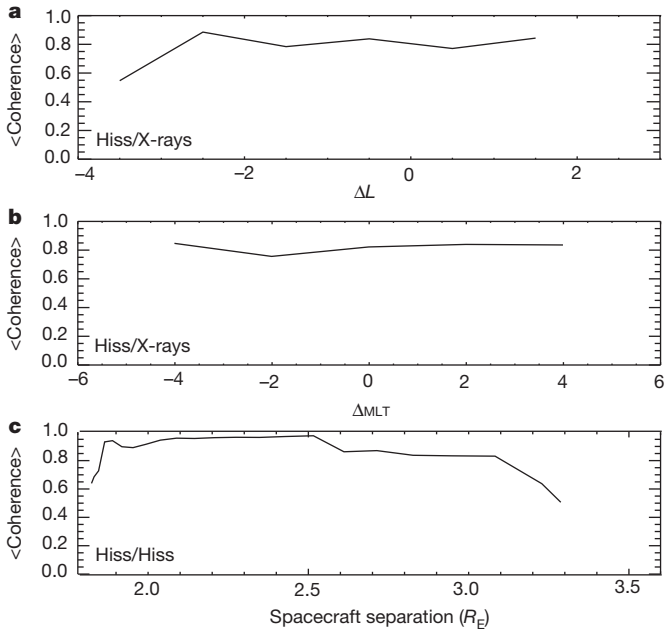

Figure 2 | The extent over which the hiss source region is modulated. Time-dependent coherence of hiss and X-rays on 6 January 2014 at 20:00–22:00 UT was calculated as a function of cross-magnetic-field separation for a range of fluctuation periods. High coherence is observed for 1–20-min periods. This figure shows a coherence of 3.3-min period fluctuations averaged for all combinations of P_A and P_B and B_K, B_L, B_W as a function of L (**a**) and MLT (**b**). Panel **c** plots the coherence of 3.3-min period fluctuations of hiss as a function of spacecraft separation.

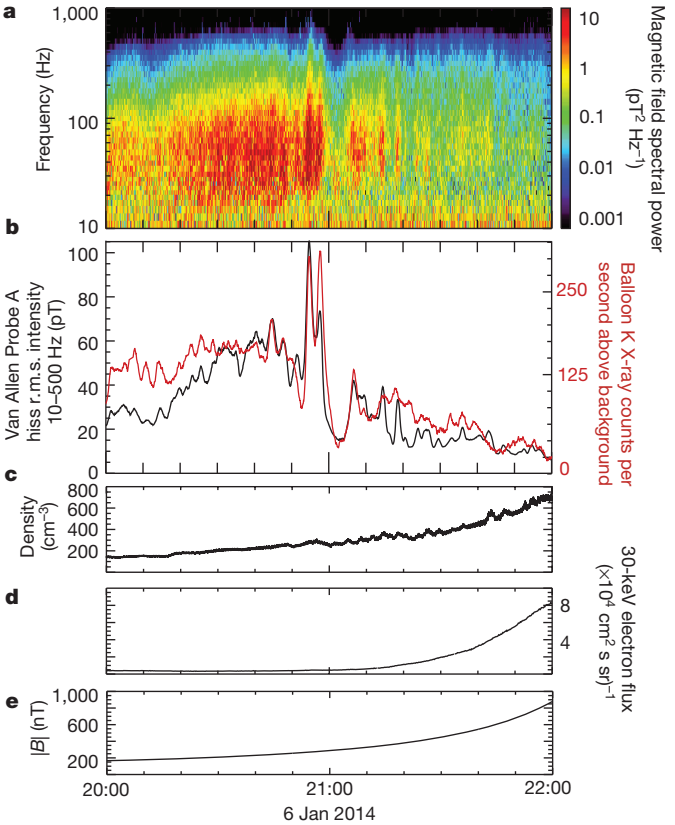

Figure 3 | Comparison of plasmaspheric hiss and electron precipitation. **a**, A spectrogram of hiss magnetic field wave power along the spin axis of P_A. The r.m.s. hiss power and X-ray count rate on B_K follow the same trend (**b**). The background X-ray count rate, probably due to cosmic-ray-induced X-rays and estimated from a 20-min running boxcar average to be 875 counts per second, has been subtracted. Plasma density, 30-keV electron flux, and magnetic field magnitude B (**c**–**e**) all increase during this conjunction, unlike for the X-ray counts.

B_W, B_L, B_X) were aloft during the 6 January 2014 conjunction and on magnetic field lines mapping to the plasmasphere. This data set allows us to quantify the spatial extent over which fluctuations of hiss and X-rays are similar. Figure 2a and b plots the average coherence (strength of association) of 3.3-min period fluctuations of hiss amplitude and X-ray count rate as a function of cross-magnetic-field separation for all combinations of a probe and a balloon. Between any two payloads, high coherence was observed for separations up to $|\Delta MLT| = 4$ h and $|\Delta L| = 3.5$. However, since high coherence was observed on all combinations of payloads, the overall coherence scale covers, at a minimum, all baselines formed by the probes and balloons: that is, 6 h of MLT (from 11:00 < MLT < 17:00) and 3.5L (from $3 < L < 6.5$). A comparison in Fig. 2c of hiss amplitudes on P_A and P_B shows that 3.3-min period fluctuations of the hiss source region are coherent on similar scales, indicating that the large-scale coherence of hiss and X-rays may be explained by the large-scale coherence of the hiss source region itself. We note that the large-scale MLT coherence is not caused by magnetic-field gradient and curvature drift of electrons into the South Atlantic Anomaly[11], a region of decreased magnetic field associated with enhanced precipitation from the radiation belts. Timescales for the drift of 30–100-keV electrons with small pitch angles, the angle of the electron velocity vector to the magnetic field, range from a few to tens of minutes per hour of MLT. Delays in fluctuations in hiss amplitude and X-ray counts of this size are not observed.

Figure 3 presents a detailed analysis of this 6 January close conjunction for the payloads P_A and B_K. As for the 3 January conjunction, hiss amplitude and X-ray count rate show a striking similarity throughout the entire two-hour conjunction. The payload separations are small near 21:00 Universal Time (UT) ($\Delta MLT = 1$ h and $\Delta L = 1.5$), meaning that these variations are mostly temporal. The plasma density and magnetic-field magnitude, as well as the 30-keV electron flux, rise on average throughout this timespan, unlike the X-ray count rate, although when detrended they fluctuate in the ultralow frequency (ULF) range, similarly to the hiss and X-rays. In a detailed analysis presented in the Methods we provide multiple lines of evidence showing that the hiss is directly responsible for creating the electron precipitation that enhances the X-rays. The global-scale coherence observed during this conjunction indicates that hiss controls electron loss throughout the afternoon-sector plasmasphere. The ULF fluctuations in density and magnetic field facilitate this process by creating conditions favourable for the growth of hiss waves. These results explain fluctuations in X-ray counts that have been observed on past balloon missions[12].

The ULF fluctuations of density and magnetic field may originate in the solar wind or at the magnetopause boundary[13], within the low-plasma-density magnetosphere[14], or within the plasmasphere[15]. We have not identified their source for the 3 January conjunction but the distinctive double-peaked feature on 6 January at 21:00 UT (Fig. 3b) is observed as a small spike in the SYM-H index, suggesting a compression at the magnetopause, and on the Cluster 4 satellite[16] located in the afternoon-sector magnetosheath. Multiple ground magnetometer stations[17] show that this ULF feature propagates throughout the afternoon-sector plasmasphere, with velocity components eastwards and radially inwards, perturbing the background density and magnetic field by a few per cent. This has a noticeable effect on the growth of plasmaspheric hiss, causing an increase in electron precipitation of up to an order of magnitude observed throughout the afternoon-sector plasmasphere all the way inward to the outer edge of the electron slot at $L = 3$, a region largely devoid of energetic electrons separating the inner and outer radiation belts.

These observations suggest that coupling models of ULF wave formation and propagation to current radiation-belt models is

important to allow accurate simulation of electron loss caused by plasmaspheric hiss during active times. Furthermore, recent results[18] have shown that plasmaspheric hiss waves are occasionally coherent and may have dispersive frequency signatures. Many models assume featureless, broadband hiss, which does not accurately describe pitch-angle scattering of electrons due to coherent, dispersive hiss waves. Coherent hiss waveforms are most prevalent during times when the plasmasphere is driven by solar wind or magnetosheath ULF pressure fluctuations[19], similar to what produces the large-scale coherence for the 6 January conjunction.

Online Content Methods, along with any additional Extended Data display items and Source Data, are available in the online version of the paper; references unique to these sections appear only in the online paper.

Received 9 December 2014; accepted 5 May 2015.

Published online 29 June 2015.

1. Gringauz, K. I. The structure of the ionized gas envelope of Earth from direct measurements in the USSR of local charged particle concentrations. *Planet. Space Sci.* **11,** 281–296 (1963).
2. Carpenter, D. L. Whistler evidence of a ''knee'' in the magnetospheric ionization density profile. *J. Geophys. Res.* **68,** 1675–1682 (1963).
3. Lyons, R. L., Thorne, R. M. & Kennel, C. F. Pitch-angle diffusion of radiation belt electrons within the plasmasphere. *J. Geophys. Res.* **77,** 3455–3474 (1972).
4. Lyons, L. & Thorne, R. M. Equilibrium structure of radiation belt electrons. *J. Geophys. Res.* **78,** 2142–2149 (1973).
5. Millan, R. M. & Thorne, R. M. Review of radiation belt relativistic electron losses. *J. Atmos. Sol. Terr. Phys.* **69,** 362–377 (2007).
6. Mauk, B. H. *et al.* Science objectives and rationale for the Radiation Belt Storm Probes Mission. *Space Sci. Rev.* **179,** 3–27 (2013).
7. Millan, R. M. *et al.* The Balloon Array for RBSP Relativistic Electron Losses (BARREL). *Space Sci. Rev.* **179,** 503–530 (2013).
8. Li, W. *et al.* An unusual enhancement of low-frequency plasmaspheric hiss in the outer plasmasphere associated with substorm-injected electrons. *Geophys. Res. Lett.* **40,** 3798–3803 (2013).
9. Chen, L. *et al.* Generation of unusually low frequency plasmaspheric hiss. *Geophys. Res. Lett.* **41,** 5702–5709 (2014).
10. Ni, B. *et al.* Resonant scattering of energetic electrons by unusual low-frequency hiss. *Geophys. Res. Lett.* **41,** 1854–1861 (2014).
11. Pinto, O. *et al.* The South Atlantic Magnetic Anomaly: three decades of research. *J. Atmos. Sol. Terr. Phys.* **54,** 1129–1134 (1992).
12. Millan, R. M. *et al.* Understanding relativistic electron losses with BARREL. *J. Atmos. Sol. Terr. Phys.* **73,** 1425–1434 (2011).
13. Claudepierre, S. G., Hudson, M. K., Lotko, W., Lyon, J. G. & Denton, R. E. Solar wind driving of magnetospheric ULF waves: field line resonances driven by dynamic pressure fluctuations. *J. Geophys. Res.* **115,** A11202 (2010).
14. Hughes, W. J., Southwood, D. J., Mauk, B., McPherron, R. L. & Barfield, J. N. Alfven waves generated by an inverted plasma energy distribution. *Nature* **275,** 43–45 (1978).
15. Dai, L. *et al.* Excitation of poloidal standing Alfven waves through drift resonance wave-particle interaction. *Geophys. Res. Lett.* **40,** 4127–4132 (2013).
16. Escoubet, C. P., Schmidt, R. & Goldstein, M. L. Cluster—science and mission overview. *Space Sci. Rev.* **79,** 11–32 (1997).
17. Mann, I. R. *et al.* The upgraded CARISMA magnetometer array in the THEMIS era. *Space Sci. Rev.* **141,** 413–451 (2008).
18. Summers, D., Omura, Y., Nakamura, S. & Kletzing, C. A. Fine structure of plasmaspheric hiss. *J. Geophys. Res.* **119,** 9134–9149 (2014).
19. Tsurutani, B. T., Falkowski, B. J., Pickett, J. S., Santolik, O. & Lakhina, G. S. Plasmaspheric hiss properties: observations from Polar. *J. Geophys. Res.* **120,** 414–431 (2015).

Acknowledgements Special thanks to the BARREL operations team B. Anderson, N. Lavers, K. Yando, D. Milling, D. Smith, A. Liang, G. Bowers and R. Friedel, and the CARISMA ground magnetometer team K. Murphy, I. R. Mann, D. K. Milling and others. Additional thanks to W. S. Kurth, A. Y. Ukhorskiy, K. Kersten and J. W. Bonnell.

Author Contributions This Letter was written by A.W.B., who performed most of the data processing and analysis. A.H. calculated diffusion coefficients and interpreted BARREL data. Additional assistance with analysis and interpretation was provided by R.M., J.S., M.McC. and L.W. (for BARREL work), J.F. (for MagEIS work), G.H. and C.A.K. (for EMFISIS work), J.R.W., C.A.C. and D.M. (for the Electric Fields and Waves instrument work) and J.G. (who performed plasmapause simulations).

Author Information Reprints and permissions information is available at www.nature.com/reprints. The authors declare no competing financial interests. Readers are welcome to comment on the online version of the paper. Correspondence and requests for materials should be addressed to A.W.B. (awbrenem@gmail.com).

METHODS

In the absence of external electric fields, magnetospheric electrons have helical trajectories, which are the result of gyration about the magnetic field and translation of the centre of this gyration—the guiding centre—along the magnetic field. The cone of velocity vectors representing these two motions is inclined from the magnetic field by an angular distance called the pitch angle. As electrons propagate along magnetic field lines towards higher latitudes, they encounter a mirror force, caused by the convergence of magnetic field lines, that opposes their guiding-centre velocity. For electrons with pitch angles outside what is called the bounce loss cone, this force is sufficient to reverse their guiding-centre motion before they reach the atmosphere. These electrons are trapped locally within the magnetosphere, bouncing between mirror points in opposite hemispheres. Electrons with pitch angles inside the bounce loss cone reach the atmosphere before mirroring and are lost from the radiation belts.

Extended Data Fig. 1 illustrates a typical conjunction between a BARREL balloon and the Van Allen probes P_A and P_B. P_A resides on a magnetic field line inside of the balloon field of view. Electrons scattered into the bounce loss cone by hiss waves within this field of view enter the atmosphere, where they create bremsstrahlung X-rays visible to the conjugate balloon. P_B resides outside of the field of view and bounce-loss-cone electrons at this location will not be observed on the balloon unless some intermediate process modulates electron loss over long distances across the magnetic field. We now discuss the mechanism by which this scattering occurs and why ULF-period enhancements of plasma density and decreases in magnetic field provide this modulation and enhance the loss rate.

Plasmaspheric hiss interacts with electrons via a Doppler-shifted cyclotron resonance. This interaction can scatter trapped electrons into the bounce loss cone, removing them from the radiation belts. Strong resonance occurs when an electron, propagating with a guiding centre velocity $\boldsymbol{V}$ towards a hiss wave with frequency f in the plasma frame, defined in terms of the angular frequency as $f = \omega/2\pi$ and wavenumber $\boldsymbol{k}$, observes the hiss wave Doppler-shifted to an integral multiple n of its gyration frequency, that is, the cyclotron frequency $f_{ce} = \omega_{ce}/2\pi$. The resonance condition is given by $n\omega_{ce} = \omega - \delta\omega$, where $\delta\omega = \boldsymbol{kV}/\gamma$ is the Doppler shift and γ is the relativistic mass factor[20]. An electron in resonance is exposed to a coherent hiss magnetic and electric field and experiences a net exchange of momentum and energy with the wave. This is possible because, in a frame that is moving together with the electron-guiding centre, the counter-streaming electron and hiss wave have the same sense of rotation about the magnetic field. For interaction with typical hiss waves, the electron energy remains constant and so the change in momentum results in a change in electron pitch angle.

Since the electron guiding centre velocity is typically along the magnetic field direction, $\boldsymbol{kV} = kV\cos\theta$, where θ is the angle the wavenumber vector makes to the magnetic field, called the wave normal angle. Wave normal angles are determined on the Van Allen probes from a singular value decomposition analysis[21] supplied by the Electric and Magnetic Field Instrument Suite and Integrated Science instrument (EMFISIS)[22]. The hiss observed during the 3 and 6 January conjunctions is relatively field-aligned throughout the hiss band, with θ in the range 20°–40°. This indicates that first-order Doppler-shifted cyclotron resonance ($n = 1$) dominates higher-order resonances.

Using *in situ* values of density, magnetic field, hiss frequency and θ we determine that first-order cyclotron resonance energies range from a few tens of kiloelectronvolts up to a few hundred kiloelectronvolts for both conjunctions. Extended Data Fig. 2a shows these energies plotted as a function of L (determined from the T89 magnetic field model[23] with an input planetary index of $K_p = 1$) for P_A on 6 January. Resonance energies tend to dip during times of enhanced hiss power, primarily due to 1–20-min fluctuations in density (enhancements) and magnetic field (depressions) which are often observed at the same time. Extended Data Fig. 2b shows Magnetic Electron Ion Spectrometer (MagEIS) instrument[24] observations on P_A of differential electron flux in a range of energy channels, plotted as a function of L. Under the assumption that these fluxes do not substantially change over the duration of the conjunction, we take these values to represent the fluxes in the hiss source region at the L value of each balloon. The range of electron energies required to satisfy the local first-order cyclotron resonance condition at the location of each balloon is indicated by the shaded rectangles. B_L and B_K, which observe substantial X-ray counts, map to an area of the hiss source region where MagEIS observed enhanced electron populations at energies required for resonance. B_X, which sees only background level X-ray counts, maps to a lower L where MagEIS observed few electrons at the required higher resonance energies. A similar result is obtained for the 3 January conjunction where B_I observed substantial electron precipitation but B_W does not. Hiss scattering of electrons into the loss cone via the mechanism of Doppler-shifted first-order cyclotron resonance is therefore consistent with the balloon observations.

Each individual resonance interaction is equally likely to scatter an electron towards higher or lower pitch angle. Because electron pitch-angle distributions in the plasmasphere are typically anisotropic, with more electrons at higher than lower pitch angles, the net angular scattering over time skews towards lower pitch angles in a manner thought to be consistent with a diffusive process. The simultaneous satellite and balloon observations allow comparison of the theoretical loss rates to observed loss rates on the balloons. We now show that these two rates are compatible for the close conjunction on 6 January near 21:00 UT.

The pitch angle α through which an electron will random walk in a single bounce period T_b due to interaction with hiss is given by $\Delta\alpha = \sqrt{2\langle D_{\alpha\alpha}\rangle T_b}$, where $\langle D_{\alpha\alpha}\rangle$ is the bounce-averaged pitch-angle diffusion rate, calculated from *in situ* density, magnetic field magnitude, θ, amplitude and bandwidth[25]. We have approximated the hiss frequency spectrum with a Gaussian, centred on the frequency of peak amplitude at each time with a bandwidth determined by the minimum and maximum extent of the observed hiss wave power. The observed spectrum has an extended high-frequency tail not matched by a normal Gaussian, but for the purposes of showing the consistency between the predicted flux at P_A and the observed flux on B_K a Gaussian is sufficient. Modelled hiss waves are allowed to interact with electrons with energies from 0–200 keV and with $\alpha = 0°$–$30°$ in a static dipole magnetic field. Diffusion rates, averaged over the gyration period of the electron about the magnetic field $D_{\alpha\alpha}$, were determined at each point along the bounce path. Next, bounce-averaged diffusion rates $\langle D_{\alpha\alpha}\rangle$ were calculated as a function of energy and time by averaging the diffusion rates for electrons with pitch angles near the bounce loss cone over the entire electron bounce path. Because $\langle D_{\alpha\alpha}\rangle$ is a function of not only hiss magnetic field wave power, but also of density and background magnetic field, it is modified by the ULF-period fluctuations.

The BARREL field of view mapped to the magnetic equator is a circle of approximate diameter $1R_E$, and X-rays observed at B_K will be produced by precipitating electrons within this entire field of view. Exactly determining the overall loss rate would require knowledge of the instantaneous hiss amplitude distribution over this entire field of view, which is clearly not possible without multiple satellite measurements. We can, however, approximate the effect of such a distribution by averaging $\langle D_{\alpha\alpha}\rangle$ over the 15 min it takes P_A to cross this field of view, resulting in a scattering rate for 50-keV electrons of 10^{-4} s^{-1}. Using this time-averaged value, 50-keV electrons within the field of view of B_K will scatter an angular distance of approximately 1° over a typical bounce period of 1 s.

From MagEIS data we can estimate the number of electrons within 1° of the 4° bounce loss cone. During the conjunction near 20:58 UT the MagEIS instrument is able to make high-time-resolution measurements to within 2.5° of the bounce loss cone. Considering the time measuring each sector is small there is large error associated with these values. Good counting statistics are obtained by averaging over ten spin periods. Results indicate a range of 25–700 electrons $(\text{cm}^2\,\text{s}\,\text{sr}\,\text{keV})^{-1}$ of energy 50 keV at the bounce loss cone for a 15-min window centred on 20:58 UT. Integrating over the solid angle of electrons within 1° of the bounce loss cone gives us the number of electrons that can theoretically be scattered by the observed hiss into the loss cone in a single bounce period. Roughly half of these electrons, corresponding to 0.08–2.4 electrons $(\text{cm}^2\,\text{s}\,\text{keV})^{-1}$, will be scattered into the bounce loss cone, and the other half will be scattered towards higher pitch angles. This is the predicted loss rate in the hiss source region due to quasi-linear diffusion.

As these electrons propagate down magnetic field lines from near the magnetic equator to the atmosphere they are focused into a smaller cross-sectional area by the converging magnetic field lines, effectively increasing the differential flux by the magnetic focusing factor $A_{eq}/A_{70\ km} = B_{70\ km}/B_{eq}$, where A is the cross-sectional area of the field of view of the balloon observing the precipitation and B is the magnetic field strength. Estimates of this focusing factor range from 250 to 310 depending on the variation in field strength over the $1R_E$-diameter field of view at the magnetic equator. Thus the flux of 0.08–2.4 electrons $(\text{cm}^2\,\text{s}\,\text{keV})^{-1}$ at 50 keV scattered into the loss cone each bounce will correspond to 15–450 electrons $(\text{cm}^2\,\text{s}\,\text{keV})^{-1}$ at 70 km, the altitude where the bremsstrahlung X-rays are created. If hiss is indeed the cause of the electron loss then the flux extracted from balloon X-ray counts should be consistent with this number.

To compare this range of values with observations at B_K we invert the X-ray counts at 20:58 UT with a bremsstrahlung X-ray model. A necessary step in this process is the subtraction of the background level of X-ray counts. These can be created from at least two sources, including cosmic rays and enhanced South Atlantic Anomaly precipitation. After background subtraction we find that BARREL observed roughly 13 electrons $(\text{cm}^2\,\text{s}\,\text{keV})^{-1}$ at 50 keV at 20:58 UT. This is probably an underestimate of the true flux by a factor of approximately three, caused by the assumption by the bremsstrahlung model that precipitating electrons at an altitude of 70 km are isotropically distributed in pitch angle. This will only be the case when the limit of strong diffusion is reached, defined as where the hiss waves are able to fill the bounce loss cone completely in a quarter

bounce period. The diffusion rates calculated are much lower than this and thus only the edge of the bounce loss cone will be filled with electrons. Compensating for this factor, our estimate of 50-keV fluxes observed on B_K is in the range 26–39 $(cm^2\,s\,keV)^{-1}$. This is consistent with the predicted flux of 15–450 electrons $(cm^2\,s\,keV)^{-1}$. Thus the electron loss associated with the X-ray count rate on B_K during the close conjunction on 6 January near 21 UT can be explained by quasi-linear scattering of electrons into the loss cone by the observed hiss waves.

We end with a power spectral analysis that provides additional evidence that plasmaspheric hiss, modulated by ULF-period fluctuations in density and magnetic field, is directly responsible for precipitating the electrons that create the X-ray fluctuations. Results are presented for the 3 January conjunction because on 6 January strong hiss and X-ray peaks near 21:00 UT can dominate the spectral comparison. However, results are similar for both days. The left column in Extended Data Fig. 3 plots detrended curves of the quantities $\langle D_{\alpha\alpha}\rangle$, hiss amplitude, density, magnetic field and 54-keV electron flux, compared to detrended X-ray counts. Not only are fluctuations in X-ray counts best matched by hiss amplitude and $\langle D_{\alpha\alpha}\rangle$, but so are the spectra shown in the right column. The density and X-ray spectra compare favourably but to a lesser degree, and the magnetic field and energetic electron flux spectra are dissimilar in that they are enhanced at frequencies where the X-ray spectrum is depressed. Taken together, these comparisons indicate that the time and spectral characteristics of the hiss more closely match those of the X-ray counts than do density, magnetic field magnitude and energetic electron flux, strongly suggesting that the hiss is directly responsible for the electron loss. Despite this, enhancements in hiss amplitude tend to occur in regions of enhanced density and depressed magnetic field, which creates conditions favourable for hiss growth[26].

20. Kennel, C. F. & Petschek, H. E. Limit on stably trapped particle fluxes. *J. Geophys. Res.* **71,** 1–28 (1966).
21. Santolík, O., Parrot, M. & Lefeuvre, F. Singular value decomposition methods for wave propagation analysis. *Radio Sci.* **38,** 1010 (2003).
22. Kletzing, C. A. *et al.* The Electric and Magnetic Field Instrument Suite and Integrated Science (EMFISIS) on RBSP. *Space Sci. Rev.* **179,** 127–181 (2013).
23. Tsyganenko, N. A. A magnetospheric magnetic field model with a warped tail current sheet. *Planet. Space Sci.* **37,** 5–20 (1989).
24. Blake, J. B. *et al.* The Magnetic Electron Ion Spectrometer (MagEIS) instruments aboard the Radiation Belt Storm Probes (RBSP) spacecraft. *Space Sci. Rev.* **179,** 383–421 (2013).
25. Summers, D., Ni, B. & Meredith, N. P. Timescales for radiation belt electron acceleration and loss due to resonant wave-particle interactions: 1. Theory. *J. Geophys. Res.* **112,** A04207 (2007).
26. Li, W. *et al.* An unusual enhancement of low-frequency plasmaspheric hiss in the outer plasmasphere associated with substorm-injected electrons. *Geophys. Res. Lett.* **40,** 3798–3803 (2013).

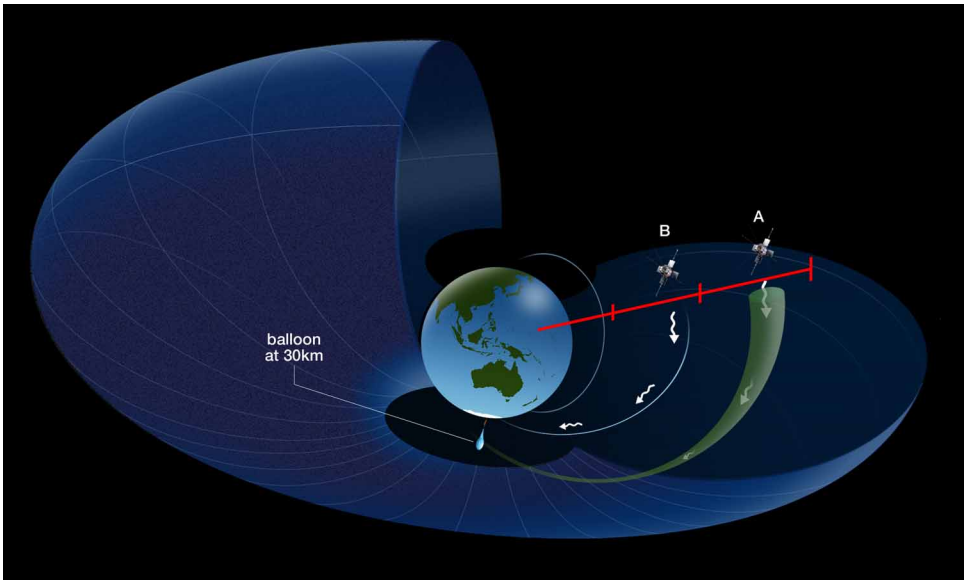

Extended Data Figure 1 | The detection of loss cone electrons by a balloon. The Van Allen probes (labelled here A and B) pass through the hiss source region at the magnetic equator ($3R_E$–$6R_E$, 40,000 km altitude) on field lines that can connect to the BARREL balloons. The red hatched line shows values of $2R_E$, $4R_E$ and $6R_E$. The shaded green volume shows the balloon field of view and the white lines represent electrons propagating along and gyrating about magnetic field lines. At an altitude of 70 km, where bremsstrahlung X-rays are typically created, the cross-section of this field of view is a circle about 100 km in radius. Mapped along magnetic field lines to the magnetic equator, this becomes a circle of radius $0.5R_E$ (about 3,200 km).

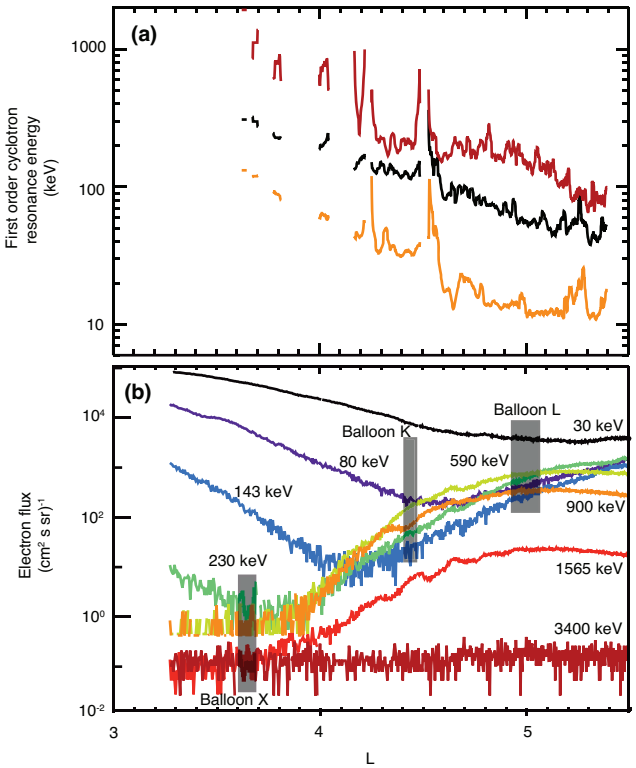

Extended Data Figure 2 | Comparison of predicted resonance energies to observed energies. **a**, Calculation of first-order cyclotron resonance energies (6 January 2014, 20:00–22:00 UT) from *in situ* data on P_A versus *L*. The three lines are resonant energies determined from the minimum (red), peak (black) and maximum hiss (orange) frequencies. **b**, MagEIS electron flux levels on P_A versus *L*. The horizontal extent of each shaded box shows the *L* crossed by the balloons. The vertical extent is a mapping of the range of resonant energies from **a** across the observed energies from MagEIS.

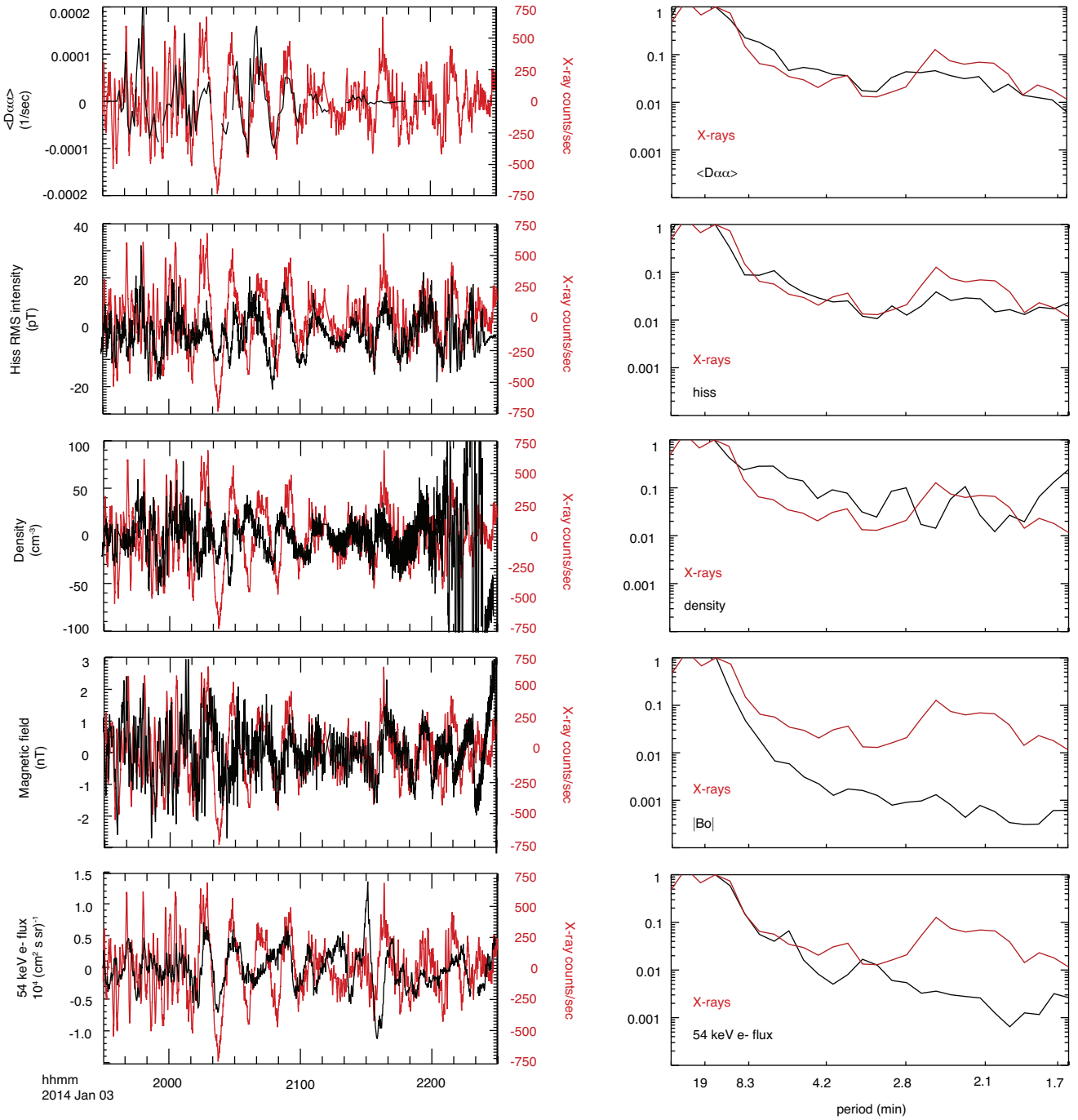

Extended Data Figure 3 | Analysis suggesting that hiss is directly responsible for observed electron loss. Coherence and power spectra from P_A and B_I of fluctuating quantity pairs $\langle D_{\alpha\alpha} \rangle$/X-rays, hiss amplitude/X-rays, magnetic field/X-rays, density/X-rays, and 54-keV electron flux/X-rays. The left plot in each row shows detrended quantity pairs while the right plot is the respective power spectral comparison for fluctuation periods from 1–20 min. To provide comparisons between spectra with different units, values are presented in decibels relative to the power of each curve at the 16.7-min period.